# Noncollinear antiferromagnetic structure of the molecule-based magnet $Mn[N(CN)_2]_2$

Carmen R. Kmety,[1] Qingzhen Huang,[2,3] Jeffrey W. Lynn,[2] Ross W. Erwin,[2] Jamie L. Manson,[4] S. McCall,[5] J. E. Crow,[5] Kenneth L. Stevenson,[6] Joel S. Miller,[4] and Arthur J. Epstein[1,7]

[1]*Department of Physics, The Ohio State University, Columbus, Ohio 43210-1106*
[2]*NIST Center for Neutron Research, National Institute of Standards and Technology, Gaithersburg, Maryland 20899*
[3]*Department of Materials and Nuclear Engineering, University of Maryland, College Park, Maryland 20742*
[4]*Department of Chemistry, University of Utah, Salt Lake City, Utah 84112-0850*
[5]*National High Magnetic Field Laboratory, 1800 East Paul Dirac Drive, Tallahassee, Florida 32310*
[6]*Department of Chemistry, Indiana University Purdue University, Fort Wayne, Indiana 46805*
[7]*Department of Chemistry, The Ohio State University, Columbus, Ohio 43210-1185*
(Received 23 February 2000)

The crystallographic and magnetic properties of the $Mn[N(CN)_2]_2$ compound have been investigated by dc magnetization, ac susceptibility, specific heat, and zero-field neutron diffraction on polycrystalline samples. The magnetic structure consists of two sublattices which are antiferromagnetically coupled and spontaneously canted. The spin orientation is mainly along the $a$ axis with a small uncompensated moment along the $b$ axis. The ground state is a crystal-field sextet with large magnetic anisotropy. The crystal structure consists of discrete octahedra which are axially elongated and successively tilted in the $ab$ plane. Comparisons of the magnetic structures for the isostructural $M[N(CN)_2]_2$ ($M$ = Mn, Fe, Co, Ni) series suggest that the spin direction is stabilized by crystal fields and the spin canting is induced by the successive tilting of the octahedra. We propose that the superexchange interaction is the mechanism responsible for the magnetic ordering in these compounds and we find that a crossover from noncollinear antiferromagnetism to collinear ferromagnetism occurs for a superexchange angle of $\alpha_c = 142.0(5)°$.

## I. INTRODUCTION

Magnetic interactions in molecule-based materials have been the subject of very active investigation in the past decade.[1] For a molecule-based magnet consisting of magnetic metal ions coordinated with nonmagnetic organic species, both the metal ions and the organic species contribute to the observed magnetism. The metal ions are the source of magnetic moments, while the organic species provide superexchange pathways between the magnetic centers. A change in the metal ions and/or superexchange pathways produces a modification of the crystal structure, which in turn may affect the magnetic ground state. Understanding the relationship between the crystal structure and magnetic ordering is crucial for the design of three-dimensional molecule-based magnets with high ordering temperatures.

$Mn[N(CN)_2]_2$ belongs to the isostructural $M[N(CN)_2]_2$ ($M$ = Mn, Fe, Co, Ni, Cu) series. Previous studies[2-13] showed that compounds with transition-metal ions having six or less electrons in the $3d$ orbitals order as canted antiferromagnets while the ones with seven or more electrons order as ferromagnets. Most of the previous work is concerned with macroscopic measurements of the bulk substance. However, to understand the effects of the crystal structure on the magnetic ordering, it is crucial to probe the systems at the microscopic level. We reported earlier that $M[N(CN)_2]_2$ ($M$ = Co, Ni) compounds have a collinear ferromagnetic structure with spin orientation along the $c$ axis.[2] In the present work, we report the magnetic structure for the $Mn[N(CN)_2]_2$ compound and discuss the possible origins of the variability of the magnetic ordering for the first row transition-metal ions compounds.

## II. EXPERIMENTAL PROCEDURES

A large ($\sim$4.5 g) batch of anhydrous $Mn[N(CN)_2]_2$ was synthesized as polycrystalline powder in two steps (in Fort Wayne). First, crystals of hydrated $Mn[N(CN)_2]_2 \cdot 3H_2O$ were obtained and then the water was removed from the crystals through pumping. $Mn(ClO_4)_2 \cdot 6H_2O$ (15.96 g, 0.0441 mol) was dissolved in 7 mL water. $Na[N(CN)_2]_2$ (9.846 g, 0.111 mol) was dissolved in 50 mL water. The room-temperature mixture of the two solutions was allowed to evaporate over several days, and crystals of $Mn[N(CN)_2]_2 \cdot 3H_2O$ began to form. The crystals were placed in a suction filter and washed with a very small amount of cold water. Then the crystals were placed in a vial with a septum which was evacuated with a vacuum pump. After several days of pumping, the crystals were transformed into a white powder and microanalyzed. The microanalysis results are: Mn, found 29.07%, calc. 29.37%; C, found 25.42%, calc. 25.69%; and N, found 44.59%, calc. 44.93%. *Perchlorate salts must be handled with extreme caution due to their explosive nature*. The crystal structure at 222 K (monoclinic, space group $P2_1/n$, $Z$=4) (Ref. 14) and magnetic properties (paramagnetic down to 5 K) of $Mn[N(CN)_2]_2 \cdot 3H_2O$ agree very well with the previously reported crystal structure at 123 K and magnetic properties.[8,9] All data presented in this paper and the isofield magnetization between 2 and 300 K reported in Ref. 6 were performed on polycrystalline samples of $Mn[N(CN)_2]_2$ from this batch. Other methods of synthesis for $Mn[N(CN)_2]_2$ are given in Refs. 8 and 9 which use the same starting materials as described above but with variations in preparation (for example, the application of heat), and Ref. 6 which uses

$MnCl_2 \cdot 4H_2O$ as starting material.

For magnetic studies, we used both the dc and ac techniques (in Columbus). The dc magnetization data were collected with a Quantum Design magnetic property measurement system (MPMS) magnetometer equipped with a superconducting quantum interference device (SQUID), a 7-T superconducting magnet and a continuous-flow cryostat. The sample was zero-field cooled from 50 to 5 K, and then the isothermal magnetization was measured for applied fields between $-5.5$ and 5.5 T. The sample was zero-field cooled (ZFC) or field cooled (FC) from 50 to 5 K, and then the isofield magnetization was recorded on warming for temperatures between 5 and 20 K. The ac susceptibility data were recorded with a Lake Shore 7225 susceptometer/magnetometer equipped with a 5-T superconducting magnet and an exchange cryostat. Phase-sensitive measurements were made using a lock-in amplifier. The linear and nonlinear (second and third harmonic) susceptibilities were measured in the temperature range from 5 to 40 K in an oscillating field of amplitude $H_{ac}=1$ Oe (linear) or 5 Oe (nonlinear) and at selected frequencies between 5 Hz and 10 kHz.

The specific-heat measurements were performed with a low mass specific-heat cryostat using a quasiadiabatic heat-pulse relaxation technique[15] (in Tallahassee). The sample, in the form of a pressed pellet of powder and with a mass of $3.8\pm0.1$ mg, was mounted on a sample holder using a small amount of Apiezon-N grease. To separate the contribution of the sample specific heat from the addenda, the specific heat of the sample holder with the grease was measured over the full temperature range prior to mounting the sample.

The neutron powder diffraction (NPD) measurements were performed on the BT-1 high-resolution powder diffractometer and BT-2 triple-axis spectrometer at the National Institute of Standards and Technology's (NIST) research reactor. To study the thermal evolution of the crystal structure, neutron-diffraction patterns were collected on BT-1 in the $2\theta$ range 3–165° at selected temperatures between 4.6 and 298 K. The incident neutron beam on BT-1 had a wavelength of $\lambda=2.0783$ Å (4.6 K) or $\lambda=1.5401$ Å (between 10 and 298 K) produced by the Ge(311) or the Cu(311) monochromator, respectively. The sample was sealed in a cylindrical vanadium container filled with He-exchange gas and mounted in a liquid He cryostat (4.6 K) or a closed-cycle He gas refrigerator (between 10 and 298 K). The crystal and magnetic structures were refined by the Rietveld method, using the General Structure Analysis System (GSAS) program[16] and adopting as initial model the room-temperature structure for $Co[N(CN)_2]_2$ derived previously.[7] To determine the zero-field (zero applied magnetic field) magnetic structure at 1.6 K, neutron-diffraction patterns were recorded on BT-2 in the $2\theta$ range 15–55° at 1.6 and 25 K. The intensities of the low-angle antiferromagnetic (AFM) Bragg peaks were monitored as a function of temperature. To study the field-dependent magnetic structure at 0.4 K, neutron-diffraction patterns of relevant Bragg peaks were collected on BT-2 in several applied fields between 0 and 6 T. The intensities of the low-angle AFM Bragg peaks were monitored as a function of external magnetic field at 0.4, 1.1, and 3.4 K. The incident neutron beam on BT-2 had a wavelength of $\lambda=2.3591$ Å, which was produced by a pyrolytic graphite

(002) monochromator and filter. The sample was sealed in a cylindrical aluminum container filled with He-exchange gas and mounted in a pumped liquid He cryostat (zero-field magnetic structure) or in a cryomagnet with a $^3$He sorption pump (field-dependent magnetic structure).

All high-resolution NPD data ($T=4.6, 10, 20, 50, 120, 200,$ and 298 K) were used for the Rietveld refinements of the crystal structures of $Mn[N(CN)_2]_2$ in the space group $Pnnm$. The background was described by a 12-parameter cosine Fourier series and the temperature factors were refined as anisotropic. At first the peak shape was modeled by a pseudo-Voigt function[17,18] which treats the diffraction peak full width at half maximum (FWHM) as a smooth function of $d$ spacing or diffraction angle $2\theta$ for a fixed-wavelength diffraction experiment. Although the peak-shape fits were improved, there were still large deviations between the observed and calculated profiles. Therefore the peak shape was described by a model recently developed by Stephens[19] which extends the above model to the case of diffraction peak FWHM that is *not* a smooth function of the $d$-spacing called *anisotropic peak-shape broadening* or *anisotropic strain broadening*. In Stephens' model, nearby peaks in a diffraction pattern have very different widths caused by a distribution of lattice parameters (of the individual crystallites) within a powder sample. A detailed explanation of the model including comparisons with previous works on anisotropic peak-shape broadening can be found in Ref. 19 and references therein. Based on the symmetry of an orthorhombic crystal system, six independent parameters ($S_{400}, S_{040}, S_{004}, S_{220}, S_{202}, S_{022}$) were introduced and refined in order to obtain optimal fits to the peaks. These parameters are uniquely determined by the widths of the peaks ($h00$), ($0k0$), ($00l$), ($hk0$), ($h0l$), and ($0kl$), respectively. The refinement results indicated that only $S_{400}, S_{040}, S_{220}$, and $S_{202}$ contributed significantly in producing excellent whole-pattern fits, which suggests that the maximum strain within the crystal is in the $ab$ plane. Other examples of systems exhibiting anisotropic peak-shape broadening for which the Rietveld refinements were greatly improved by using Stephens' model are sodium *para*-hydroxybenzoate[20] and $Rb_3C_{60}$.[19] We note that the crystal structure of $Mn[N(CN)_2]_2$ at 120 K obtained from our profile refinements [$a=6.1144(3)$ Å, $b=7.2759(2)$ Å, $c=7.5581(2)$ Å] is in very good agreement with the single-crystal x-ray solution at 123 K [$a=6.1126(3)$ Å, $b=7.2723(3)$ Å, $c=7.5563(4)$ Å].[8]

Below the transition temperature ($T_N \sim 16$ K), the high-resolution NPD patterns showed three additional peaks at low angle (inset of Fig. 1) suggesting a predominantly antiferromagnetic (AFM) ordering, and some weakly enhanced nuclear peaks. Because weak ferromagnetic (FM) peaks occur on top of strong nuclear peaks, the subtle detail of the magnetic structure of $Mn[N(CN)_2]_2$ could not be determined from Rietveld refinements of the high-resolution NPD data. Therefore the magnetic structure was first determined from high-intensity NPD studies (Sec. IV C) combined with magnetic studies (Sec. IV A), and subsequently introduced in the refinements of the high-resolution NPD data. Although the details of the magnetic structure are presented in the sections that follow, we note here that a small FM component along the $b$ axis appears to be present in the system. How-
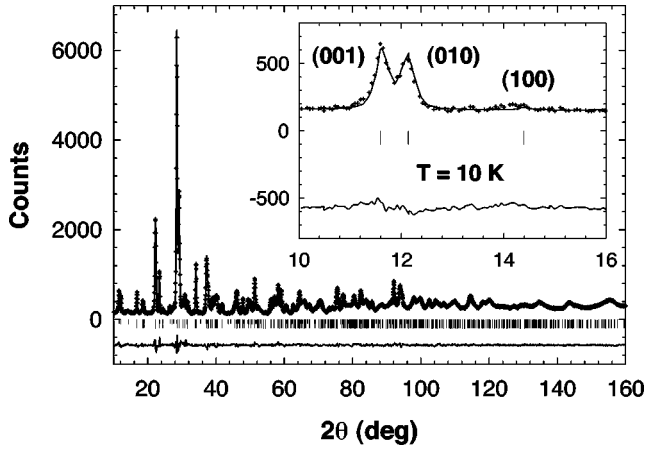
FIG. 1. Neutron-diffraction pattern at 10 K in the noncollinear antiferromagnetic state. The crosses represent the experimental intensity, the upper solid line is the calculated intensity, and the lower solid line is the difference intensity (between the observed and calculated intensities). The vertical lines mark the angular positions of the nuclear (grey) and magnetic (black) Bragg peaks. Inset: Pure magnetic Bragg peaks generated by the antiferromagnetic component of the magnetic ordering.

ever, the refinements of the magnetic structure were performed with the $b$-axis FM component fixed to zero (due to limited sensitivity).

## III. CRYSTAL STRUCTURE

The results of the diffraction refinements are presented in Figs. 1–4, and Tables I–III. The plots show an example of a Rietveld fit to the data (Fig. 1), the crystal structure (Fig. 2), and the thermal evolution of the crystal structure (Figs. 3 and 4). The tables contain structural parameters (Table I), anisotropic temperature factors (Table II), and geometrical data (Table III) for $Mn[N(CN)_2]_2$ at low (1.6 and 10 K) and room temperature. For comparison, Table III also includes
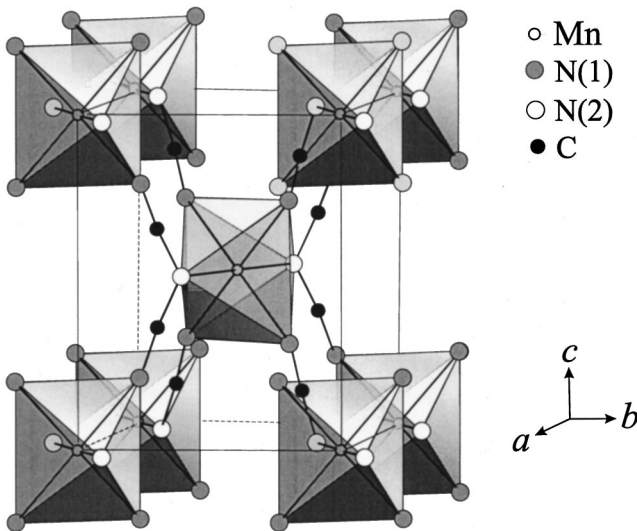


FIG. 2. The crystallographic unit cell in the paramagnetic regime as well as in the ordered state for $Mn[N(CN)_2]_2$. The structure consists of discrete $MnN_6$ octahedra which are axially elongated and successively tilted in the $ab$ plane.
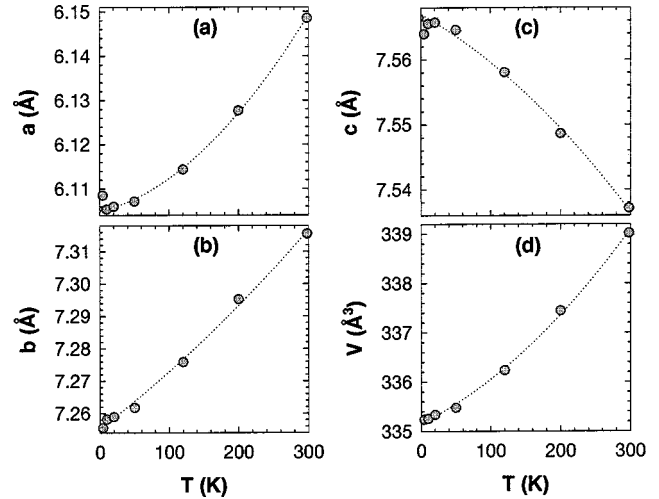


FIG. 3. Orthorhombic lattice parameters (a), (b), and (c), and unit-cell volume (d) as a function of temperature. The error bars are smaller than the plot symbols. The dotted lines are guides for the eye.

the geometrical data for the $M[N(CN)_2]_2$ ($M$ = Fe, Co, Ni) compounds at 1.6 K and room temperature.

The crystal structure of the $Mn[N(CN)_2]_2$ compound (Fig. 2) is the same as that obtained for $M[N(CN)_2]_2$ ($M$ = Fe,[5] Co,[2,3,7] Ni[2,3,7]) compounds. It consists of hinged rhombus-shaped repeats of $Mn[N(CN)_2]_2$ that form "chains" parallel to the $c$ axis. There are two (symmetry related) Mn ions in the orthorhombic unit cell, one located at $(0,0,0)$ (corner) and the other located at $(1/2,1/2,1/2)$ (center). Each Mn ion is coordinated to six nitrogen atoms in the form of an axially elongated octahedron [$4 \times$ Mn-N(1) and $2 \times$ Mn-N(2)]. The long axes of the octahedra are contained in the $ab$ plane and are tilted by the same angle but in opposite senses of rotation about the $c$ axis. The successive tilting of the octahedra in the $ab$ plane may be the source of strain evidenced by the anisotropic peak-shape broadening of the NPD pattern. We show that these lattice distortions, i.e., the axial elongation and successive tilting of the octahedra in the $ab$ plane, play a crucial role in the resulting magnetic structure (Sec. V).

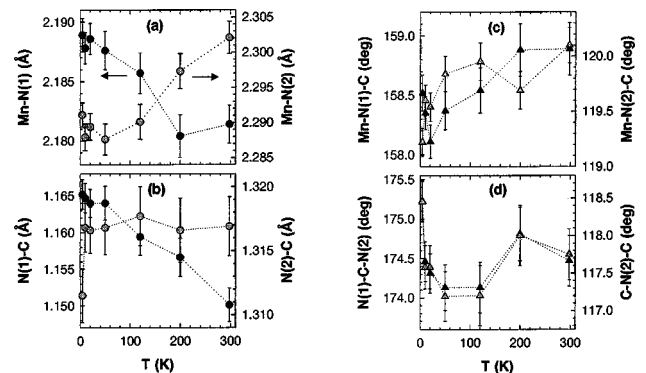The thermal evolution of the orthorhombic lattice param-



FIG. 4. Selected bond lengths (a) and (b), and bond angles (c) and (d) as a function of temperature. The black (grey) symbols are represented on the left (right) axes. The dotted lines are guides for the eye.

TABLE I. Structural parameters, magnetic parameters, and conventional reliability factors for $Mn[N(CN)_2]_2$ at selected temperatures, obtained from the Rietveld refinement of the high-resolution neutron-diffraction data.

| $T$ (K) | 4.6 | 10 | 298 |
|---|---|---|---|
| Space group | $Pnnm$ | $Pnnm$ | $Pnnm$ |
| $a$ (Å) | 6.1085(2) | 6.1054(2) | 6.1486(4) |
| $b$ (Å) | 7.2555(2) | 7.2582(2) | 7.3155(3) |
| $c$ (Å) | 7.5640(1) | 7.5655(2) | 7.5371(2) |
| $V$ (Å$^3$) | 335.24(1) | 335.26(1) | 339.02(3) |
| Mn $(2a)$[b] $(0,0,0)$[c] | | | |
| C $(8h)$[b] $(x,y,z)$[c] | | | |
| $x$ | $-0.2721(4)$ | $-0.2718(4)$ | $-0.2646(5)$ |
| $y$ | 0.1434(3) | 0.1425(3) | 0.1460(3) |
| $z$ | 0.3510(3) | 0.3511(2) | 0.3504(3) |
| N(1) $(8h)$[b] $(x,y,z)$[c] | | | |
| $x$ | $-0.2189(2)$ | $-0.2190(2)$ | $-0.2131(3)$ |
| $y$ | 0.0885(1) | 0.0886(1) | 0.0935(2) |
| $z$ | 0.2128(2) | 0.2125(2) | 0.2128(2) |
| N(2) $(4g)$[b] $(x,y,1/2)$[c] | | | |
| $x$ | $-0.3454(3)$ | $-0.3463(3)$ | $-0.3358(4)$ |
| $y$ | 0.2123(2) | 0.2125(3) | 0.2172(3) |
| Mn-N(1) ($\times 4$)[d] | 2.189(1) | 2.188(1) | 2.181(2) |
| Mn-N(2) ($\times 2$)[d] | 2.291(2) | 2.288(2) | 2.302(2) |
| N(1)-C ($\times 1$)[d] | 1.165(2) | 1.165(2) | 1.150(2) |
| N(2)-C ($\times 2$)[d] | 1.312(2) | 1.317(2) | 1.317(2) |
| N(1)-Mn-N(2) | 90.9(1) | 91.0(1) | 91.1(1) |
| N(1)-Mn-N(2) | 89.1(1) | 89.0(1) | 88.9(1) |
| Mn-N(1)-C | 158.5(2) | 158.4(1) | 158.9(2) |
| Mn-N(2)-C | 119.2(1) | 119.6(1) | 120.1(2) |
| C-N(2)-C | 118.5(3) | 117.6(3) | 117.8(3) |
| N(1)-C-N(2) | 175.2(3) | 174.5(3) | 174.5(3) |
| Mn | | | |
| $\mu_x$ ($\mu_B$) | 4.34(4) | 3.82(4) | |
| $\mu_y$ ($\mu_B$) | 0[a] | 0[a] | |
| $\mu_z$ ($\mu_B$) | 1.66(9) | 0.96(18) | |
| $\mu$ ($\mu_B$) | 4.65(4) | 3.94(4) | |
| $\vartheta$ (°) | 69(1) | 76(3) | |
| $\varphi$ (°) | 0[a] | 0[a] | |
| $R_p$ (%) | 3.72 | 3.56 | 2.78 |
| $R_{wp}$ (%) | 4.96 | 4.29 | 3.41 |
| $\chi^2$ | 1.731 | 2.111 | 1.684 |

[a]Very small parameters, which were fixed to zero during the final refinement.
[b]Site symmetries.
[c]Atomic positions, where the numbers indicate special-symmetry positions.
[d]Bond multiplicity.

TABLE II. Anisotropic temperature parameters for $Mn[N(CN)_2]_2$ at selected temperatures, obtained from the Rietveld refinement of the high-resolution neutron-diffraction data.

| $T$ (K) | 4.6 | 10 | 298 |
|---|---|---|---|
| Mn | | | |
| $B_{11}$ (Å$^2$) | 0[a] | 2.26(39) | 3.17(49) |
| $B_{22}$ (Å$^2$) | 1.96(35) | 0.89(29) | 1.73(38) |
| $B_{33}$ (Å$^2$) | 0[a] | 0[a] | 1.26(33) |
| $B_{12}$ (Å$^2$) | $-0.23(30)$ | 0.98(28) | $-0.29(38)$ |
| $B_{13}$ (Å$^2$) | 0 | 0 | 0 |
| $B_{23}$ (Å$^2$) | 0 | 0 | 0 |
| C | | | |
| $B_{11}$ (Å$^2$) | 2.53(19) | 1.80(13) | 3.32(20) |
| $B_{22}$ (Å$^2$) | 1.25(11) | 1.06(8) | 2.81(11) |
| $B_{33}$ (Å$^2$) | 0.31(14) | 0.38(8) | 2.18(11) |
| $B_{12}$ (Å$^2$) | 0.36(9) | 0.12(8) | 0.05(12) |
| $B_{13}$ (Å$^2$) | $-0.43(11)$ | 0.06(9) | 0.73(10) |
| $B_{23}$ (Å$^2$) | $-0.40(9)$ | $-0.09(5)$ | $-0.17(7)$ |
| N(1) | | | |
| $B_{11}$ (Å$^2$) | 1.78(10) | 1.63(8) | 4.66(14) |
| $B_{22}$ (Å$^2$) | 1.95(10) | 1.53(7) | 4.45(11) |
| $B_{33}$ (Å$^2$) | 1.13(8) | 1.05(5) | 2.23(7) |
| $B_{12}$ (Å$^2$) | 0.42(8) | 0.002(64) | 0.09(11) |
| $B_{13}$ (Å$^2$) | 0.07(7) | 0.43(7) | 0.98(10) |
| $B_{23}$ (Å$^2$) | $-0.11(7)$ | $-0.04(5)$ | $-0.57(6)$ |
| N(2) | | | |
| $B_{11}$ (Å$^2$) | 2.04(15) | 1.45(13) | 5.36(22) |
| $B_{22}$ (Å$^2$) | 1.28(11) | 1.75(10) | 3.51(15) |
| $B_{33}$ (Å$^2$) | 0.58(15) | 1.01(9) | 1.90(10) |
| $B_{12}$ (Å$^2$) | $-0.29(10)$ | 0.32(9) | 1.25(13) |
| $B_{13}$ (Å$^2$) | 0 | 0 | 0 |
| $B_{23}$ (Å$^2$) | 0 | 0 | 0 |

[a]Very small parameters, which were fixed to zero during the final refinement.

eters and unit-cell volume are presented in Fig. 3. The volume of the unit cell decreases smoothly with temperature, which indicates that no structural phase transitions accompany the magnetic ordering down to 4.6 K. The $b$ axis decreases monotonically with temperature, but the $a$ and $c$ lattice parameters show an anomalous behavior with temperature. From room temperature to about 10 K, $a$ exhibits positive thermal expansion while $c$ exhibits negative thermal expansion. At 10 K, a sign reversal of the thermal expansion occurs for these lattice parameters. The fractional changes in length between 10–300 K and 4.6–10 K are: $\Delta a/a = +0.71$ and $-0.05\%$, $\Delta b/b = +0.79$ and $+0.04\%$, and $\Delta c/c = -0.38$ and $+0.02\%$. The change in the direction of variation of the $a$ and $c$ lattice parameters may be related to the development of the ordered Mn moment components along the same axes. In contrast, the temperature variation of the $b$ axis component is very small below $T_N$, which leaves the monotonic behavior of the $b$ axis unaffected. The anomalous behavior of the crystal structure may be the origin of the shoulder in the specific heat at about 7 K (Sec. IV B) and the

TABLE III. Interatomic distances (in Å) and angles (in deg) for $M[N(CN)_2]_2$ ($M$ = Mn, Fe, Co, Ni) at low and room temperature, calculated with the parameters given in Table I for $M$ = Mn, Ref. 5 for $M$ = Fe, and Ref. 2 for $M$ = Co, Ni. $\Delta$ is the octahedral distortion parameter defined as $\Delta = M\text{-N}(2)/M\text{-N}(1)$, (Ref. 21) $\beta$ is the tilt angle of the equatorial plane of the $M\text{N}_6$ octahedron from the $ac$ plane, and $2\beta$ is the dihedral angle between the equatorial planes of the octahedra surrounding the nearest-neighbor metal ions.

| $M^{2+}$ | $T$ (K) | $M$-$M$ | $M$-N(2)-$C$ | N(2)-$C$-N(1) | $C$-N(1)-$M$ | $\alpha$ | $M$-N(1) | $M$-N(2) | $\Delta$ | $\beta$ |
|---|---|---|---|---|---|---|---|---|---|---|
| Mn$^{2+}$ | 4.6 | 6.0657(1) | 119.2(1) | 175.2(3) | 158.5(2) | 140.4(1) | 2.189(1) | 2.291(2) | 1.047 | 25.2(2) |
| | 10 | 6.0662(1) | 119.6(1) | 174.5(3) | 158.4(1) | 140.2(1) | 2.188(1) | 2.288(2) | 1.046 | 25.2(2) |
| | RT | 6.0854(2) | 120.1(2) | 174.5(3) | 158.9(2) | 141.1(1) | 2.181(2) | 2.302(2) | 1.055 | 27.1(2) |
| Fe$^{2+}$ | 1.6 | 5.9670(1) | 119.6(1) | 175.5(2) | 158.9(1) | 141.7(1) | 2.126(1) | 2.206(1) | 1.038 | 26.4(2) |
| | RT | 5.9846(1) | 119.5(1) | 176.3(2) | 159.5(1) | 142.7(1) | 2.126(1) | 2.219(2) | 1.044 | 27.8(2) |
| Co$^{2+}$ | 1.6 | 5.9158(1) | 120.6(1) | 175.1(2) | 159.6(1) | 142.3(1) | 2.093(1) | 2.156(2) | 1.030 | 27.5(2) |
| | RT | 5.9360(1) | 120.7(1) | 175.3(2) | 160.3(1) | 143.1(1) | 2.095(1) | 2.162(2) | 1.032 | 28.9(2) |
| Ni$^{2+}$ | 1.6 | 5.8634(1) | 121.0(1) | 174.6(2) | 159.5(1) | 142.6(1) | 2.053(1) | 2.129(2) | 1.037 | 27.6(2) |
| | RT | 5.8798(1) | 120.7(1) | 175.2(2) | 159.8(2) | 143.5(1) | 2.053(1) | 2.140(2) | 1.043 | 28.9(2) |

change in the trend of the magnetic order parameter of the (100) peak at about the same temperature (Sec. IV C).

Figure 4 shows selected internal structural parameters as a function of temperature. The largest effects are observed in the bond lengths as opposed to bond angles. The MnN$_6$ octahedra remain axially elongated and successively tilted in the $ab$ plane at all temperatures studied. The two axial (long) Mn-N(2) bond lengths (in the $ab$ plane) contract while the four equatorial (short) Mn-N(1) bond lengths (along the chain) expand between 298 and 4.6 K [Fig. 4(a)]. The net effect is a less distorted octahedron as evidenced by the octahedral distortion parameter $\Delta = M\text{-N}(2)/M\text{-N}(1)^{21}$ (Table III). The rhombus-shaped repeat of the chain (along the $c$ axis) consists of two Mn-N(1) and four cyano (two single and two triple) bonds on each side. On cooling, the Mn-N(1) and the single bond lengths expand, while the triple bond length is independent of temperature down to 10 K [Fig. 4(b)]. At the same time, some of the bond angles of the repeat decrease [Mn-N(1)-C, Fig. 4(c)] and others remain constant [C-N(2)-C, Fig. 4(d)]. The expansion of the bond lengths along the chain may be responsible for the negative thermal expansion of the $c$ axis down to 10 K. At 10 K, the contraction of the triple bonds by 0.4% [Fig. 4(b)] may be enough to reverse the sign of the thermal expansion of the $c$ axis. The symmetry-related Mn ions are connected as Mn-N(2)-C-N(1)-Mn. The N(1)-C-N(2) angle is essentially independent of temperature [Fig. 4(d)]. The angles connecting the Mn ions to their common neighbor [N(1)-C-N(2)] decrease slightly with temperature [Fig. 4(c)]. We consider N(1)-C-N(2) as a rigid entity.

To gain insight into the origins of the variability of the magnetic ordering in the isostructural series $M[N(CN)_2]_2$ ($M$ = Mn, Fe, Co, Ni), we have gathered in Table III the geometrical parameters relevant to the magnetic interaction. Since the compounds are insulating magnetic systems, the magnetic interactions between nearest-neighbor magnetic ions are either direct exchange (DE) or superexchange (SE).[22] Since the distance between neighboring ions ($M$-$M$) is large, the coupling due to DE is expected to be negligibly small. Therefore SE interaction is the principal mechanism for the magnetic ordering in this series. The nearest-neighbor

SE pathway proceeds through $M$-N(2)-C-N(1)-$M$, which is contained in the diagonal plane perpendicular to the $ab$ plane. The two angles [$M$-N(1)-C, $M$-N(2)-C] that connect the metal ions to the rigid unit [N(1)-C-N(2)] decrease slightly with temperature. It appears that the changes of the two angles sum up to give the change in the angle $M$-C-$M$ (denoted by $\alpha$ in Table III). Therefore we selected $\alpha$ to represent the superexchange angle between the nearest-neighbor metal ions (Sec. V). Finally, $\Delta$ and $\beta$ are used to describe the distortion and rotation of the $M\text{N}_6$ octahedra. $\Delta$ is the octahedral distortion parameter,[21] $\beta$ is the tilt angle of the equatorial plane from the $ac$ plane, and $2\beta$ is the dihedral angle between the equatorial planes of the octahedra surrounding the nearest-neighbor metal ions.

## IV. MAGNETIC ORDERING

### A. dc magnetization and ac susceptibility

The in-field magnetic measurements, isofield dc susceptibility $\chi_{dc}(T)$ ($2 \leqslant T \leqslant 300$ K) and isothermal magnetization $M(H)$ ($-5.5 \leqslant H \leqslant 5.5$ T) at 5 K, suggest a canted antiferromagnetic state, through the presence of a small ferromagnetic component superposed on an overall antiferromagnetic behavior. In Ref. 6, we presented the temperature dependence of $\chi_{dc}(T)$ as the product of dc susceptibility with temperature $\chi_{dc}T(T)$. On cooling from room temperature to 16.1 K, the product $\chi_{dc}T(T)$ decreases indicating AFM correlations at high temperatures. As the temperature is lowered further, an unexpected rapid increase develops with a maximum of 6.2 emu Oe/mol at 12.2 K. The FM component is the peak at 12.2 K, which is characteristic to FM transitions. The high-temperature data yield a Curie constant corresponding to a spin $S = 5/2$ and a Landé factor $g_S = 1.98$. Figure 5(a) shows the isothermal magnetization as a function of the applied field at 5 K, in the low-field region. The small FM component has a hysteresis loop with a coercive field of 0.08 T. Outside this low-field region, the isothermal magnetization is linear showing no saturation at the highest measured field of 5.5 T [$M(5.5$ T$) = 5400$ emu Oe/mol]. The linear magnetization vs applied field is a characteristic of simple AFM.
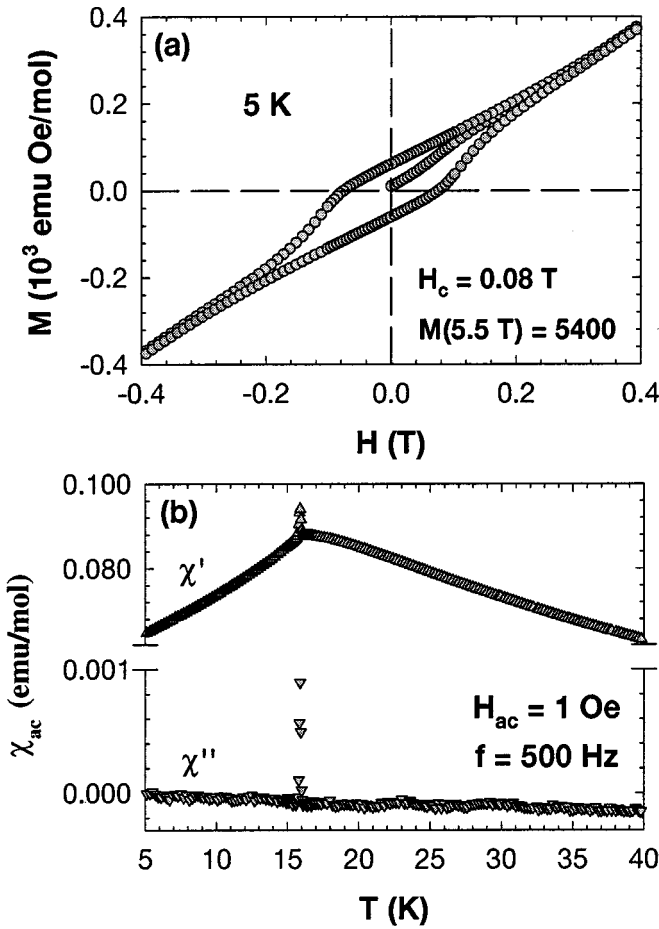
FIG. 5. (a) Isothermal magnetization as a function of applied field at 5 K. The coercive field is 0.08 T and the magnetization at 5.5 T is 5400 emu Oe/mol. (b) Real or in-phase ($\chi'$) and imaginary or out-of-phase ($\chi''$) components of the *zero-field* ac susceptibility ($\chi_{ac}$) as a function of temperature, measured in an oscillating field of amplitude, $H_{ac} = 1$ Oe, and frequency, $f = 500$ Hz. Measurements at selected frequencies (not shown) between 5 Hz and 10 kHz yielded similar data.

The zero-field ac susceptibility $\chi_{ac}(T)$ ($5 \leq T \leq 40$ K) demonstrates that a small ferromagnetic component is also present in the system when no magnetic field ($H_{dc} = 0$) is applied. Figure 5(b) shows the real $\chi'(T)$ and imaginary $\chi''(T)$ components in a driving field of amplitude 1 Oe and frequency 500 Hz. Note the spikes in $\chi'(T)$ and $\chi''(T)$ at 15.9 K and 15.8 K, respectively. The spikes arise from the small FM component and their positions denote the transition temperature $T_N$.[23] The triangular shape of $\chi'(T)$ and the absence of $\chi''(T)$ are typical for simple AFM behavior. Another example of a $Mn^{2+}$ magnetic system with similar zero-field $\chi_{ac}(T)$ data is $(n\text{-}C_3H_7NH_3)_2MnCl_4$.[24] Measurements of $\chi_{ac}$ at selected frequencies between 5 Hz and 10 kHz showed no frequency shift of $T_N$, which indicates that glassiness does not coexist with the ordered state.[25] The second harmonic susceptibility is zero, as expected for simple AFM, except for a spike arising at the transition temperature due to the small FM component present in the system. Since the FM component of the magnetic ordering in $Mn[N(CN)_2]_2$ appears to be smaller than the sensitivity of the NPD experiments (Sec. IV C), the zero-field $\chi_{ac}$ data are
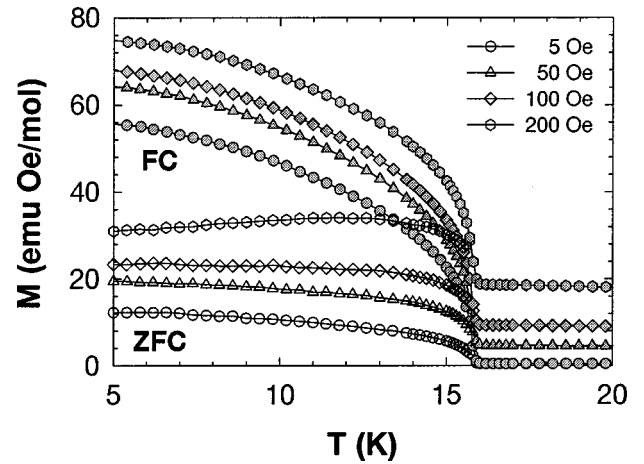


FIG. 6. Zero-field-cooled (ZFC, open symbols) and field-cooled (FC, closed symbols) magnetization as a function of temperature, measured in different applied magnetic fields.

the only experimental evidence that supports the canting of the Mn moments in the absence of an applied magnetic field.

The zero-field-cooled (ZFC) and field-cooled (FC) magnetization curves (Fig. 6) vanish at the transition temperature of $T_N = 16.0(2)$ K. The bifurcation temperatures defined by the onset of irreversibilities are independent of the applied field, which confirms that there is no glassy behavior in the system.[25]

Recently, some of the magnetic data of $Mn[N(CN)_2]_2$ were reported by other authors for samples prepared by various methods.[8] In order to construct an accurate microscopic model for the low-temperature magnetic structure, systematic studies (including magnetic, specific heat, and neutron diffraction) on samples from a single batch are necessary. In the present work, we report systematic studies on samples from a single batch.

### B. Specific heat

The specific-heat measurements confirm the transition temperature and type of magnetic ordering obtained from magnetic (Sec. IV A) and NPD (Sec. IV C) studies. Figure 7(a) shows the zero-field specific heat $C(T)$ collected between 1.8 and 25 K. The essential features of the data are a $\lambda$ peak at 15.62 K followed by a large specific heat "tail." The $\lambda$ peak is associated with the magnetic phase transition from a paramagnet to a canted antiferromagnet, while the large tail is due to lattice vibrations and short-range order (see below). In addition, a weak shoulder appears to be present at about 7 K, which may be connected to the observed anomalous behavior of the crystal structure below 10 K (Sec. III). The application of a large magnetic field of 12 T [Fig. 7(b)] affects the $\lambda$ peak. The peak position was shifted down from 15.6 to 14.3 K, while the peak height was reduced from 31.8 to 25.4 J/mol K. Since the shift of the ordering peak to low (high) temperatures is characteristic of AFM (FM) transitions,[26] the in-field results are consistent with predominantly AFM ordering below the transition temperature. The zero-field specific-heat data were measured by other authors on a sample prepared by a different method.[8] Although the overall shape of our zero-field $C(T)$ data is similar to the shape presented in Ref. 8, the height of our $\lambda$ peak
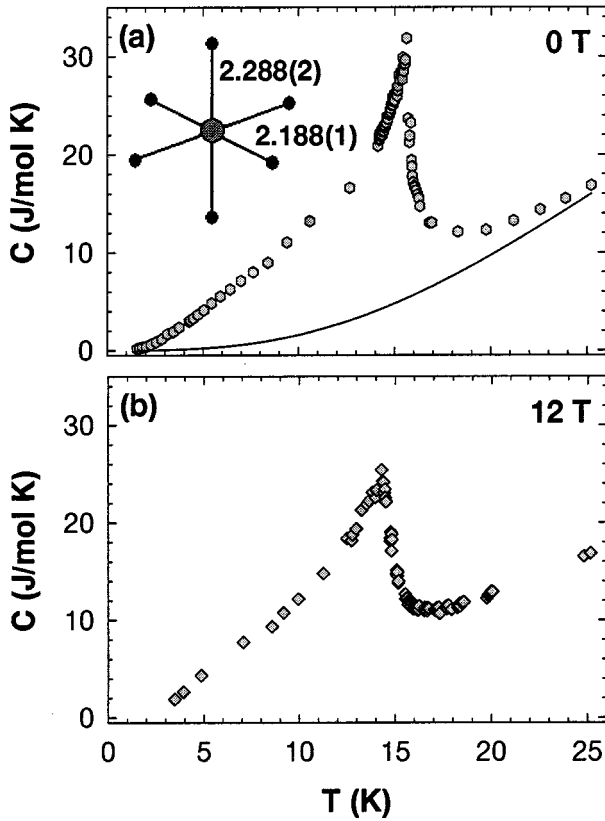
FIG. 7. Specific heat as a function of temperature, measured in an applied magnetic field of (a) 0 T and (b) 12 T. The solid line is the estimated lattice specific heat. (Ref. 4 and 27). Inset: A schematic drawing of the geometry around the $Mn^{2+}$ ion, which is an elongated octahedron with two axial bond lengths of 2.288(2) Å and four equatorial bond lengths of 2.188(1) Å at 10 K. For $Mn^{2+}$ in an elongated octahedron, a negative zero-field splitting is expected to occur.
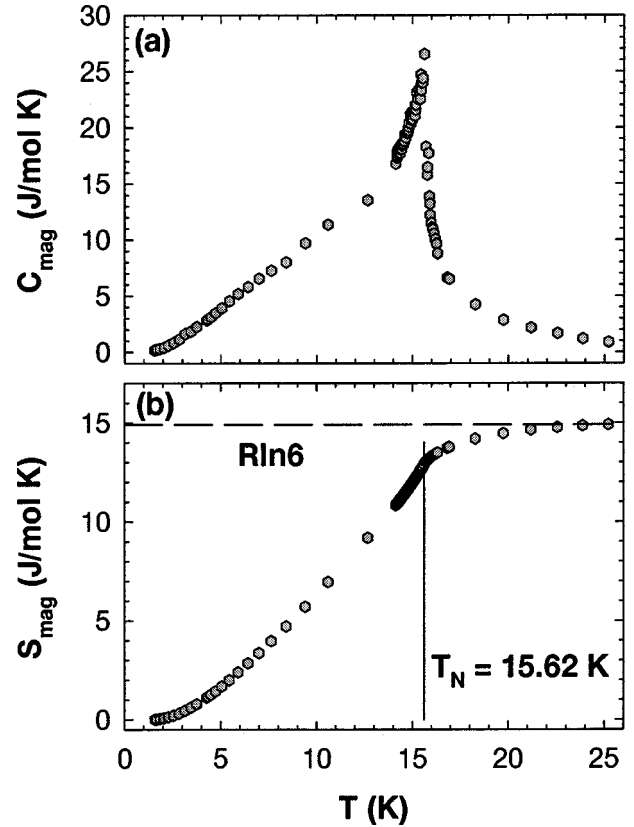


FIG. 8. (a) Magnetic specific heat as a function of temperature, obtained by subtracting the lattice specific heat from the total. (b) Magnetic entropy as a function of temperature, obtained by integrating the magnetic specific heat versus $d(\ln T)$. The data yield a transition entropy of $R \ln 6$ corresponding to $S = 5/2$.

(31.8 J/mol K) is about twice the height observed in Ref. 8 (16 J/mol K). The lower height of the $\lambda$ peak in Ref. 8 may be due to the presence of some other (nonmagnetic) products in the sample[8] rather than different magnetic phenomena.

The magnetic ground state is a crystal-field sextet with large magnetic anisotropy. Since $Mn[N(CN)_2]_2$ is an insulating magnetic system, the zero-field data $C(T)$ data are well described by a model consisting of a magnetic specific heat $C_{mag}(T)$ and a lattice specific heat $C_{lat}(T)$. The $C_{lat}(T)$ [Fig. 7(a), solid line] was estimated by the corresponding states approximation,[27] making use of the specific heat of the isomorphous paramagnetic $Cu[N(CN)_2]_2$.[4] Although this is a paramagnetic compound, the measured zero-field specific heat gave no evidence for any magnetic ordering effects above 1.8 K. The same method of estimating $C_{lat}(T)$ was used in Refs. 28 and 29 (with a paramagnetic isomorph) and Refs. 30–33 (with a diamagnetic isomorph). Figure 8(a) shows $C_{mag}(T)$ obtained by subtracting $C_{lat}(T)$ from $C(T)$. By integrating $C_{mag}(T)$ with respect to $d(\ln T)$ [Fig. 8(b)] and $dT$ (not shown), we determined the magnetic entropy $S_{tot}$ (total magnetic entropy change below and above $T_N$) and magnetic energy $E_{tot}$ (total magnetic energy change below and above $T_N$), respectively. The experimental data yielded a magnetic entropy of $S_{tot} = R \ln 6$, which shows that the AFM ordering arises from a crystal-field sextet ($S$

$=5/2$). The critical entropy $S_c$ (entropy change below $T_N$) is about 87% of $S_{tot} = R \ln 6$. Comparisons of the experimental $S_c$ with the theoretical predictions for the three-dimensional (3D) Ising (80% of $S_{tot}$), $XY$ (64% of $S_{tot}$), and Heisenberg (62% of $S_{tot}$) models,[23] and 2D Ising (44% of $S_{tot}$),[34] suggest that the system can be described by a 3D Ising-like magnetic model. From the experimental $E_{tot} = 163$ J/mol, we extracted an exchange parameter of $J/k_B = E_{tot}/(RS^2z) = -0.39$ K, which agrees well with $J/k_B = 3T_N/[2S(S+1)z] = -0.34$ K obtained from mean-field theory.[35] Lower values of the magnetic entropy $S_{tot} = 5.76$ and 10.1 J/mol K have been observed for samples prepared according to Refs. 6 and 8, respectively. However, the value of $S_{tot} = 14.9$ J/mol K extracted from our data agrees well with the *theoretically* expected magnetic entropy of $S_{tot} = R \ln(2S+1) = R \ln 6$ where $S$ is the effective spin of the paramagnetic ion in the ground state, and with the *experimental* value of the manganese moment $\mu(Mn^{2+}) = g_S S = 4.61(1) \ \mu_B$ obtained from NPD studies (Sec. IV C). Both low-temperature techniques applied to samples reported here, the specific heat and neutron diffraction, are consistent with an $S = 5/2$ system.

The anisotropy in the magnetic ground state is due to a relatively large negative zero-field splitting (ZFS) compared to most $Mn^{2+}$ compounds, which results in a large single-ion anisotropy (SIA). The free $Mn^{2+}$ ion has a $3d^5$ electronic configuration, which gives rise to a $^6S$ ground state. In an octahedral crystalline field (CF), the orbital ground state is

$^6A_{1g}$. Based on the crystal structure, the $Mn^{2+}$ ion resides at the center of an axially distorted octahedron [see inset of Fig. 7(a)]. For an axially distorted CF, the SIA may be represented by a $D(S_z^2)$ term [where $D$ is the (axial) ZFS parameter] in the Hamiltonian. Through the combined effect of the axially distorted CF and second-order spin-orbit (SO) coupling, the spin sextet of the $^6A_{1g}$ level is split into three Kramers doublets ($|\pm 1/2\rangle$, $|\pm 3/2\rangle$, and $|\pm 5/2\rangle$). Since the axial distortion is elongation, $D<0$ (Ref. 36) and the $|\pm 5/2\rangle$ level lies lower. The value of $S_{tot}=R\ln 6$ indicates that the doublet-doublet separations (which are proportional to the magnitude of $D$) are small compared with $T_N$. As a result, at low temperature all three doublets are thermally populated and the system behaves as an effective spin $S=5/2$ system. Based on the definitions of the anisotropy field $H_A$, the exchange field $H_E$, spin-flop transition field extrapolated to 0 K $H_{SF}(0)$,[23] and the experimental finding[5] that $H_{SF}(0)=0.52$ T, we estimate the magnitude of $D/k_B \simeq 4 \times 10^{-3}$ K. It is also possible to estimate the ratio $H_A/H_E \simeq 10^{-3}$, which is a relative measure of the ideality of the isotropic exchange interaction.[23] The value of $H_A/H_E$ for $Mn[N(CN)_2]_2$ is comparable to $H_A/H_E=1.6 \times 10^{-2}$ for $MnF_2$, but is much larger than $H_A/H_E=5 \times 10^{-6}$ of $RbMnF_3$.[23] The $MnF_2$ system has been interpreted as a 3D Heisenberg system with large magnetic anisotropy or a 3D Ising-like system, while $RbMnF_3$ is a 3D isotropic Heisenberg system.[23,34] Hence $Mn[N(CN)_2]_2$ is ascribed to be a 3D Heisenberg system with large magnetic anisotropy.

### C. Zero-field magnetic structure

At 1.6 K $Mn[N(CN)_2]_2$ is an antiferromagnet characterized by a magnetic unit cell equal to the crystallographic unit cell in which the magnetic moments of the two manganese ions [one located at $(0,0,0)$ and the other at $(1/2,1/2,1/2)$] are slightly tilted from the $a$ axis. The comparison of the neutron-diffraction patterns measured at 1.6 K [Fig. 9(a)] and 25 K [Fig. 9(b)] reveals both the appearance of new magnetic Bragg peaks as well as magnetic peaks that occur at the same positions as the nuclear Bragg peaks. The peaks containing magnetic contributions are indexed as (001), (010), (100), (111), overlapping (012) and (021), and overlapping (112), (121), (201), and (210) in the crystallographic unit cell. The low-angle magnetic peaks, (001), (010), and (100), are *pure* magnetic peaks; i.e., these peaks do not occur at the same positions as the nuclear peaks. The presence of the pure magnetic peaks indicates that the body-centered unit cell consists of two simple manganese sublattices (defined by the corner and center ions) which are AFM coupled. The (001) and (010) peaks have comparable integrated intensities, while the (100) peak is much weaker. Since the (100) peak receives contributions solely from the $\mu_y$ and $\mu_z$ components of the magnetic moment $\mu$, we conclude that these components must be small.

The spin orientation with respect to the crystallographic axes for *one* magnetic sublattice is given by the spherical coordinates $\vartheta=77(3)°$ and $\varphi=10(6)°$, and the corresponding magnitude of the magnetic moment per manganese ion is $\mu(Mn^{2+})=4.61(1)\mu_B$. The subtraction of the 25 K data [Fig. 9(b)] from the 1.6 K data [Fig. 9(a)] yielded the mag-
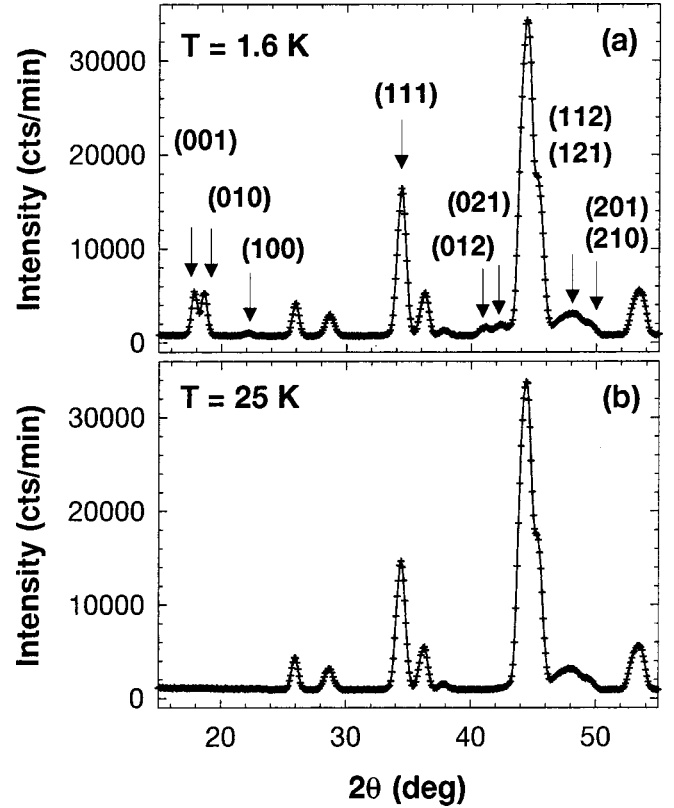


FIG. 9. Neutron-diffraction pattern at (a) 1.6 K in the ordered state, and (b) 25 K in the paramagnetic regime. The crosses represent the experimental intensity and the solid lines are guides for the eye. The arrows indicate the Bragg peaks that are either new or enhanced due to the magnetic intensity developed in the ordered state.

netic diffraction pattern, which consists of six magnetic peaks with their scattering angles lying between $17 \leq 2\theta \leq 50°$. General details of the subtraction technique were presented in Refs. 2 and 37. From these six magnetic peaks (enumerated in the previous paragraph and marked by arrows in Fig. 9(a), only the best magnetic peaks (Fig. 10) were used in the determination of the spin orientation and magnitude of the magnetic moment. For all calculations the magnetic moments were assumed to be localized on the manganese ions. The experimental integrated intensities and positions of the magnetic and nuclear Bragg peaks were obtained by fitting a resolution-limited Gaussian to each peak. The calculated integrated intensities of the magnetic peaks were obtained by using Eqs. (3) and (4) from Ref. 38. For the magnetic form factor of the manganese ion we used the calculated free-ion value.[39] The orientation of the spins was determined by finding the best agreement between the ratios of the integrated intensities of the magnetic Bragg peaks in the experimental diffraction pattern and the patterns calculated for spin orientations with $\vartheta$ and $\varphi$ varying between 0° and 90° in steps of 1°. The magnetic diffraction pattern at 1.6 K with the above method yielded $\vartheta=77(3)°$ and $\varphi=10(6)°$, which are close to the values $\vartheta=69(1)°$ and $\varphi=0°$ obtained from the Rietveld refinement of the 4.6 K high-resolution NPD pattern (Table I). The magnitude of the magnetic moment was extracted from the magnetic integrated intensities of the (001), (010), and (111) peaks, which were placed on an absolute
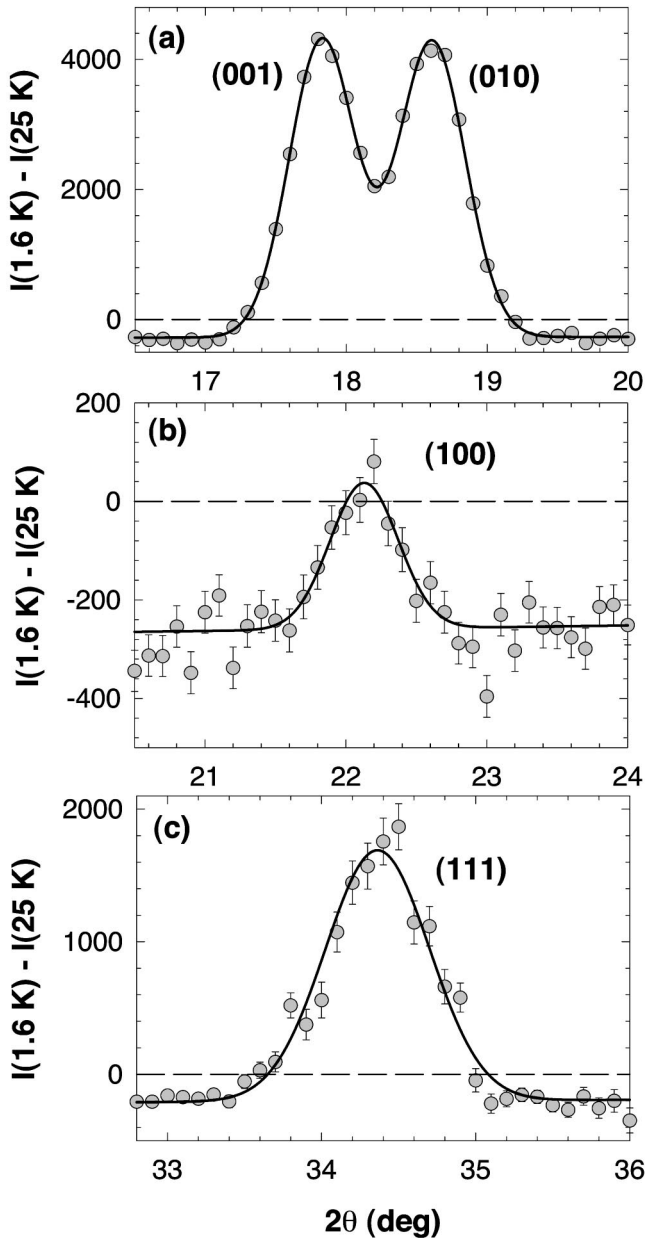
FIG. 10. Part of the magnetic diffraction pattern, obtained by subtracting the 25 K data from the 1.6 K data of Fig. 9. The solid lines are Gaussian fits to the peaks.
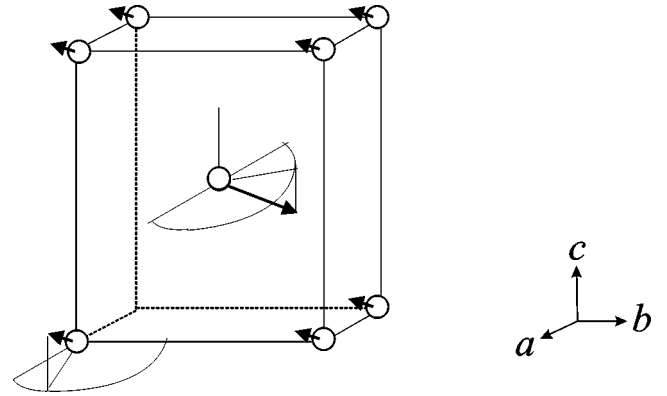


FIG. 11. Configuration of the $Mn^{2+}$ magnetic moments in the unit cell. The corner and center arrows have same lengths, but they appear of different lengths due to the perspective view.

the two manganese moments. The inspection of the *zero-field* magnetic diffraction pattern indicates that reliable peaks with $h+k+l=$ even are *not* present within our experimental error. Therefore the *zero-field* ac susceptibility measurements play a crucial role in establishing that the system has a FM (uncompensated) component to the magnetic ordering (Sec. IV A). Since the FM component is below the resolution of our NPD experiments, it must originate from the small canting angle of the two manganese sublattices. Other examples of noncollinear AFM systems characterized by small canting angles that could not be detected by NPD experiments are presented in Refs. 44 and 45. We note that for a canted AFM the large component(s) are compensated and at least one of the small components is uncompensated.

At 1.6 K and in zero applied field, the model that best describes the system has the uncompensated component to the magnetic ordering along the $b$ axis (Fig. 11). Based on the small experimental integrated intensity of the (100) peak and the calculated values for $\vartheta=77(3)°$ and $\varphi=10(6)°$, the components $\mu_y$ and $\mu_z$ are small. Therefore for our system to be a canted AFM, $\mu_y$ and $\mu_z$ are the only components that could be uncompensated. In other words, the FM component could be along the $b$ axis, $c$ axis, or in the $bc$ plane (i.e., along both $b$ and $c$ axes). We know that the magnetic (100) peak receives contributions solely from the $\mu_y$ and $\mu_z$ components which are AFM. Hence the presence of the (100) peak rules out the possibility of the FM component to be in the $bc$ plane. Consistency is obtained from the magnetic symmetry which only allows the FM component to be either along the $c$ axis (magnetic space group $*Pn'n'm$) or in the $ab$ plane (magnetic space group $*Pnn'm'$) for a FM described by the nuclear space group $Pnnm$.[46] Our study of the evolution of the spin orientation in applied magnetic field[5] indicates that the $\mu_z$ component is increasing with the field but the overall behavior is still AFM. For the system to remain a canted AFM in a large magnetic field, the $\mu_z$ component must be compensated. The above analysis leaves the FM component to the magnetic ordering along the $b$ axis as the only possibility.

The magnitude of the $b$ axis FM component increases with $\varphi$. From the high-intensity NPD data, we calculated that $\varphi=10(6)°$. The absence of the FM peaks in the magnetic diffraction pattern (Fig. 10) suggests that the calculated value of $\varphi$ might be too large. In order to determine a more appro-

scale by comparison with the nuclear integrated intensity of the (111) peak.[40,41] The value $\mu(Mn^{2+})=4.61(1)\mu_B$ is somewhat lower than the theoretically expected free ion value of $5\mu_B$ (for $S=5/2$ and $g_S=2.00$), which may be due to partial spin delocalization onto the ligands. Other $Mn^{2+}$ magnetic systems exhibiting a moment reduction are $Cu_2MnSnS_4$ $[4.28(4)\mu_B]$[42] and $MnTe_2$ $[4.28(4)\mu_B]$.[43] For the manganese ions belonging to different magnetic sublattices, the magnitudes of the magnetic moments are assumed to be identical since the local environment around each of the two manganese ions in the unit cell is identical.

The orientation of the two manganese sublattices with respect to each other is canted (or noncollinear, $\nearrow\searrow$) as opposed to tilted (or collinear, $\nearrow\diagup$). For a body-centered magnetic unit cell, the magnetic Bragg peaks with $h+k+l$ = odd (even) are generated by the AFM (FM) components of
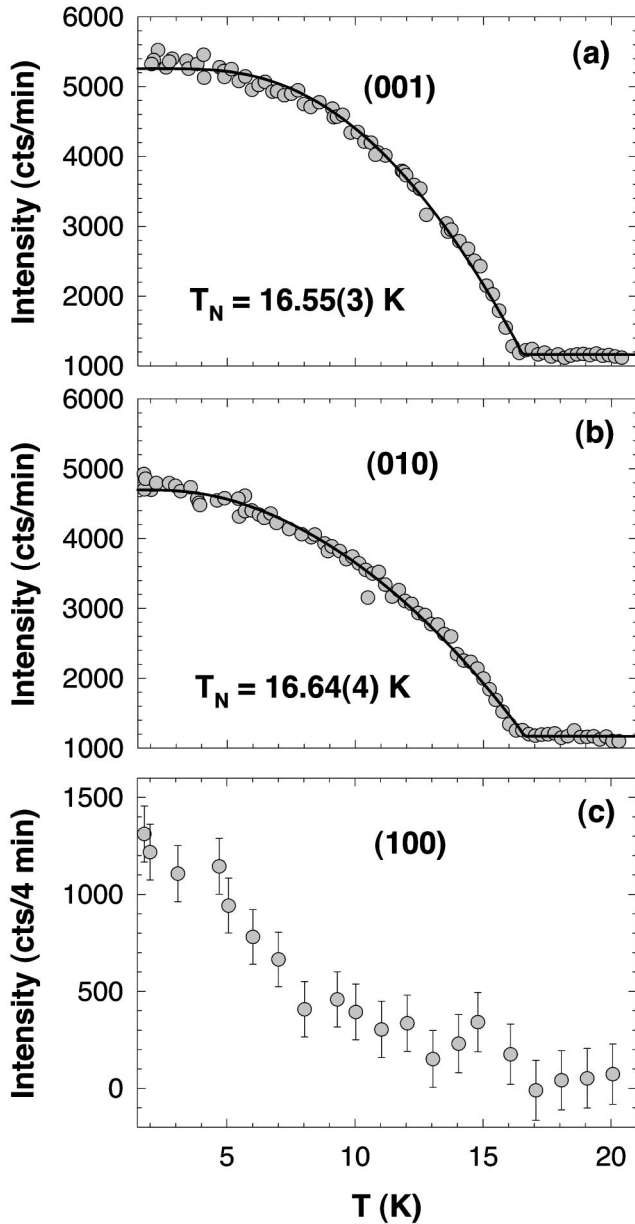
FIG. 12. Experimental intensity as a function of temperature for the three pure magnetic Bragg peaks (a) (001), (b) (010), and (c) (100). The solid lines are Brillouin function fits to the data.

priate upper limit for $\varphi$, the structure factors of the magnetic Bragg peaks for $5° \leqslant \varphi \leqslant 10°$ were calculated. For $\varphi = 5°$ the structure factors of all FM peaks are about one order of magnitude smaller than the structure factor of the weakest AFM peak [Fig. 10(b)], which would make the FM peaks unobservable. Therefore a *nonzero* value of $\varphi$ lower than $\simeq 5°$ is consistent with the ac susceptibility as well as the NPD studies. We note that $2\varphi$ is the canting angle between the two manganese sublattices.

Measurements of the magnetic order parameter reveal that some magnetic anisotropy is present in the system and confirm the transition temperatures obtained from magnetic and specific heat studies. Figure 12 shows the experimental intensity as a function of temperature of the three pure magnetic peaks. According to Eqs. (3) and (4) of Ref. 38, the integrated intensity of each magnetic Bragg peak is propor-

tional to the square of the ordered moment. Therefore, Fig. 12 describes the behavior of the square of the magnetic moment per manganese ion with temperature. The shape of the data for the (001) peak [Fig. 12(a)] and (010) peak [Fig. 12(b)] is typical for a magnetic order parameter[22,23] and is similar to the field-cooled magnetization presented in Fig. 6. In contrast, the shape of the data for the (100) peak is quite unusual, exhibiting an abrupt change in trend around 7 K. Similar behavior has been observed by Batten *et al.*[8] for the same system in the field-cooled bulk magnetization data. We note that the change in trend at about 7 K in the NPD data may be connected to the observed anomalous behavior of the crystal structure below 10 K (Sec. III). The difference in the temperature dependence of the AFM peaks suggests that the magnetic interactions are anisotropic. To obtain an estimate of the transition temperature, we fitted Brillouin functions to the data [Figs. 12(a) and (b), solid lines] by varying the exchange constant, $T_N$ and saturation magnetization. The fitted ordering temperatures are 16.55(3) K for (001) and 16.64(4) K for (010), which are in good agreement with the values obtained from the magnetization and specific-heat measurements.

## V. DISCUSSION

In the following, we attempt to qualitatively explain the differences in the: (i) sign of the exchange coupling, (ii) spin orientation, and (iii) spin canting for the isostructural $M[N(CN)_2]_2$ [$M = $ Mn (this work), Fe,[5] Co,[2] Ni[2]] series.

In insulating compounds of the transition-metal ions, the most important source of magnetic exchange interactions between the metal ions is assumed to be the superexchange (SE) interaction.[22] The SE interaction between two nearest-neighbor magnetic ions is mediated by the electrons in their common nonmagnetic neighbors; i.e., the SE interaction proceeds by means of cation-anion-cation pathways. The sign and relative strengths of the SE interactions depend on the amount of atomic orbital overlap of the metal ions corresponding to different structural configurations. Mechanisms describing the SE interaction have been proposed by Anderson,[47] Goodenough,[48] and Kanamori[49] for the special cases of 180° and 90° cation-anion-cation angle or SE angle ($\alpha$), which provide qualitative criteria (AGK rules) of determining the signs and strengths of SE interactions.

To gain insight into the contributing factors to the *sign* of SE interaction, we discuss the Anderson mechanism.[47,49] Based on the symmetry relations between the cation and anion orbitals, electron transfer, or partial covalent bonds can be formed between either the $d\epsilon$ (alternate notation $t_{2g}$) and $p\pi$ orbitals, the $d\gamma$ (alternate notation $e_g$) and $p\sigma$ orbitals, or the $d\gamma$ and $s$ orbitals of the cation and anion, respectively. In the Anderson mechanism, an electron (allowed by the Pauli principle) is first transferred from the $p\sigma$ orbital to one of the neighboring cations (via $p\sigma$-$d\gamma$ bond) and then the electron is replaced by one of like spin from the other neighboring cation (via $p\sigma'$-$d\gamma'$ bond). It is useful to attribute a sign to the partial covalent bond and to the exchange integral between the cation and anion. The bond is positive (negative) if the unpaired spin left on the anion is parallel (antiparallel) to the spin of the bonding cation. The average exchange integral is positive (negative) for orthogonal

(nonorthogonal) orbitals between the cation and anion. The sign of the SE interaction is the product of the sign of the bond and the sign of the exchange integral between cation and anion. Anderson mechanism predicts a decrease of FM interactions with decreasing number of the $3d$ electrons.

In the $M[N(CN)_2]_2$ ($M=$ Mn, Fe, Co, Ni) compounds, the SE interaction proceeds through cation-anion-cation $(M\text{-}[N(2)\text{-}C\text{-}N(1)]\text{-}M)$ pathways of *intermediate* SE angles ($\alpha$), where the rigid unit N(1)-C-N(2) represents the anion. In this case, additional partial covalent bonds are formed between the $d\epsilon$ and $d\gamma$ orbitals of $M^{2+}$ with the $p\sigma$, $p\pi$, and $s$ orbitals of $[N(CN)_2]^-$. The electronic configuration of the lowest orbital state of $M^{2+}$ in (nondistorted) octahedral geometry is given by: $d\epsilon^3 d\gamma^2$ for $Mn^{2+}$, $(d\epsilon^2)d\epsilon^2 d\gamma^2$ for $Fe^{2+}$, $(d\epsilon^4)d\epsilon^1 d\gamma^2$ for $Co^{2+}$, and $(d\epsilon^6)d\gamma^2$ for $Ni^{2+}$, where the parentheses indicate paired electrons. Based on the relative number of unpaired electrons, the stronger bonds involve the $d\epsilon$ orbital for $Mn^{2+}$ and $d\gamma$ orbital for $Co^{2+}$ and $Ni^{2+}$. The sign of the bonds is positive for all four metal ions. The sign of the SE interaction is negative for $Mn^{2+}$ and $Fe^{2+}$ ions and positive for $Co^{2+}$ and $Ni^{2+}$ ions. According to Anderson mechanism (if applicable), the overlapping orbitals are on average nonorthogonal for $M[N(CN)_2]_2$ ($M=$ Mn, Fe) and orthogonal for $M[N(CN)_2]_2$ ($M=$ Co, Ni). The prediction of Anderson mechanism that FM interactions decrease with decreasing number of the $3d$ electrons appears to be valid for the $M[N(CN)_2]_2$ series. Another example for which the prediction seems to work is the transition-metal dichlorides (layered materials) series, for which nearest-neighbor (in-plane) exchange interaction is AFM for less-than-half-filled $3d$ orbitals and FM for the rest.[50] Based on similar arguments as presented above, Goodenough[48] proposed that the coupling between the same ions must change from FM to AFM for a crossover value of the SE angle ($\alpha_c$). Theoretical studies[51] confirm Goodenough's suggestion.

In the $M[N(CN)_2]_2$ ($M=$ Mn, Fe, Co, Ni) series, the sign of the SE interaction depends on the magnitude of the SE angle. Table III summarizes the low-temperature values of the SE angles for the metal ions spanning the magnetic ordering crossover region. By substituting the metal ion while keeping the same ligand, from $Mn^{2+}$ (largest radius) to $Ni^{2+}$ (smallest radius), the crystal structure remains the same (same space group, different bond lengths and bond angles) but the magnetic ordering changes from canted AFM to FM for a crossover angle $\alpha_c=142.0(5)°$. The gradual decrease of the ion's radius results in a gradual increase of the SE angle which in turn induces a crossover from canted AFM to FM ground state. Hence we can structurally tune the magnetic ground state in this series. A similar study has been performed by Subramanian *et al.*[26] on the perovskite $SeCuO_3$, in which the gradual substitution of $Se^{4+}$ (small radius) with $Te^{4+}$ (large radius) resulted in a crossover from FM to AFM ground state at a crossover angle of $\alpha_c = 127.0(5)°$.

The orientation of the spins with respect to the crystallographic axes is most likely determined by the distorted crystal fields surrounding the metal ions. Since the $Mn^{2+}$ is an $S$-state ion, the magnetic anisotropy in $Mn[N(CN)_2]_2$ is expected to be small.[23] However, our experimental findings show the contrary: the critical entropy corresponds to a 3D

Ising-like model (Sec. IV B) and the intensity of the (100) peak vs temperature exhibits unusual behavior [Sec. IV C, Fig. 12(c)]. Large magnetic anisotropy is also present in $M[N(CN)_2]_2$ ($M=$ Fe,[5] Co,[2,7] Ni[2,7]). The main feature common to all three systems is a large zero-field splitting, which is due to the axial distortion of the octahedra surrounding the metal ions. Table III summarizes the equatorial $M$-N(1) and axial $M$-N(2) bond lengths of the $MN_6$ octahedra, and the octahedral distortion parameter $\Delta = M\text{-}N(2)/M\text{-}N(1)$[21] for $M[N(CN)_2]_2$ ($M=$ Mn, Fe, Co, Ni). It is worth noting that $\Delta$ is largest for the Mn system. Similar interpretations have resulted from a theoretical investigation by Sachidanandam *et al.*[52] of the isostructural series $R_2CuO_4$ with $R=$ Nd, Pr, Sm for which the rare-earth moments of Nd and Pr (Ref. 53) are perpendicular to the moments of Sm.[54] Other sources of anisotropy like exchange and dipole-dipole interactions are expected to be less significant.

The spin canting in $Mn[N(CN)_2]_2$ is attributed to structural effects rather than other sources of canting like the Dzyaloshinsky-Moriya (DM) interaction or frustration of magnetic interactions. The occurrence of spin canting in a system is limited by the symmetry requirement that the magnetic moments in one unit cell are not related by a center of inversion.[23] In spite of the fullfilement of the above symmetry requirement by the crystal structures of $M[N(CN)_2]_2$ ($M=$ Mn, Co, Ni), only the $Mn^{2+}$ moments are canted while the $Co^{2+}$ and $Ni^{2+}$ moments are not. The most commonly invoked explanations for canting are the DM interaction[55] and frustration.[56] Since the magnitude of the DM interaction is proportional to $(g_J-2)/2$ and $g_J=1.98$ for $Mn^{2+}$, 5.34 for $Co^{2+}$, and 2.21 for $Ni^{2+}$, the DM interaction is expected to be weakest for $Mn^{2+}$. The frustration of magnetic interactions is produced by either the geometry of the magnetic lattice for an AFM on some form of a triangular lattice, or the randomly distributed competing FM/AFM interactions. Based on the structural studies for $M[N(CN)_2]_2$ ($M=$ Mn, Co, Ni) (Sec. III), the spin sites are all occupied (no site disorder) and the magnetic lattices are not assembled of triangles or tetrahedra (no geometric frustration). According to the magnetic studies for $M[N(CN)_2]_2$ ($M=$ Mn, Co, Ni) (Secs. IV A and IV C), there is no evidence of randomly distributed competing FM/AFM interactions (no bond disorder). In a mathematical way we can define the frustration function as $\Phi = \Pi \; \mathrm{sgn}(J_{ij}) = \pm 1$, where the minus sign denotes a frustrated system.[25] Since the number of magnetic ions in each group of nearest neighbors (first, second, third, . . . ) is even, $\Phi = (-1)^4 (+1)^2 \cdots = +1$ for all three systems. These observations suggest that the most important source of spin canting is the opposite tilting of the $MN_6$ octahedra from one unit cell about the $c$ axis.[23] Table III gives the tilt angle of the equatorial plane of the $MN_6$ octahedra from the $ac$ plane. The $Mn^{2+}$ moments lie almost in the plane where tilting occurs ($ab$ plane) while the $Co^{2+}$ and $Ni^{2+}$ moments are perpendicular to it (along the $c$ axis). As a result, the $Mn^{2+}$ moments are affected while the $Co^{2+}$ and $Ni^{2+}$ moments are not. Another example of a system for which the opposite tilting of the octahedra plays an important role in the canting of the spins is $CsCoCl_3 \cdot 2H_2O$.[23]

To quantitatively explain the origins for the variability of the magnetic structures in $M[N(CN)_2]_2$ series, theoretical

investigations of the energetics of these magnetic structures using a microscopic model are needed.

[1] *Proceedings of the 6$^{th}$ International Conference on Molecule-Based Magnets*, edited by O. Kahn (Gordon and Breach, Amsterdam, 1999); *Molecule-Based Magnetic Materials: Theory, Techniques, and Applications*, edited by M.M. Turnbull, T. Sugimoto, and L.K. Thompson, ACS Symposium Series Vol. 644 (Am. Chem. Soc., Washington DC, 1996).

[2] C.R. Kmety, J.L. Manson, Q. Huang, J.W. Lynn, R.W. Erwin, J.S. Miller, and A.J. Epstein, Phys. Rev. B **60**, 60 (1999).

[3] C.R. Kmety, J.L. Manson, Q. Huang, J.W. Lynn, R.W. Erwin, J.S. Miller, and A.J. Epstein, Mol. Cryst. Liq. Cryst. Sci. Technol., Sect. A **334**, 631 (1999).

[4] C.R. Kmety, J.L. Manson, S. McCall, J.E. Crow, K.L. Stevenson, J.S. Miller, and A.J. Epstein (unpublished).

[5] C.R. Kmety, Q. Huang, J.W. Lynn, R. W. Erwin, S. McCall, J. E. Crow, K.L. Stevenson, J.S. Miller, and A.J. Epstein (unpublished).

[6] J.L. Manson, C.R. Kmety, A.J. Epstein, and J.S. Miller, Inorg. Chem. **38**, 2552 (1999).

[7] J.L. Manson, C.R. Kmety, Q. Huang, J.W. Lynn, G.M. Bendele, S. Pagola, P.W. Stephens, L.M. Liable-Sands, A.L. Rheingold, A.J. Epstein, and J.S. Miller, Chem. Mater. **10**, 2552 (1998).

[8] S.R. Batten, P. Jensen, C.J. Kepert, M. Kurmoo, B. Moubaraki, K.S. Murray, and D.J. Price, J. Chem. Soc. Dalton Trans. **1999**, 2987.

[9] K.S. Murray, S.R. Batten, B. Moubaraki, D.J. Price, and R. Robson, Mol. Cryst. Liq. Cryst. Sci. Technol., Sect. A **335**, 313 (1999).

[10] S.R. Batten, P. Jensen, B. Moubaraki, K.S. Murray, and R. Robson, Chem. Commun. (Cambridge) **1998**, 439.

[11] M. Kurmoo and C.J. Kepert, New J. Chem. **22**, 1515 (1998).

[12] M. Kurmoo and C.J. Kepert, Mol. Cryst. Liq. Cryst. Sci. Technol., Sect. A **334**, 693 (1999).

[13] H. Koehler, A. Kolbe, and G. Lux, Z. Anorg. Allg. Chem. **428**, 103 (1979).

[14] The crystal structure at 222 K of $Mn[N(CN)_2]_2 \cdot 3H_2O$ was solved by J. Gallucci, Department of Chemistry, The Ohio State University, Columbus, OH 43210, and deposited at the Cambridge Crystallographic Data Centre with deposition number CCDC 140250.

[15] R. Bachmann, F.J. DiSalvo, Jr., T.H. Geballe, R.L. Greene, R.E. Howard, C.N. King, H.C. Kirsch, K.N. Lee, R.E. Schwall, H.U. Thomas, and R.B. Zubeck, Rev. Sci. Instrum. **43**, 205 (1972).

[16] A.C. Larson and R.B. Von Dreele, *General Structure Analysis System*, Los Alamos National Laboratory Report No. LAUR-86-748, 1990.

[17] P. Thompson, D.E. Cox, and J.B. Hastings, J. Appl. Crystallogr. **20**, 79 (1987).

[18] L.W. Finger, D.E. Cox, and A.P. Jephcoat, J. Appl. Crystallogr. **27**, 892 (1994).

[19] P.W. Stephens, J. Appl. Crystallogr. **32**, 281 (1999).

[20] R.E. Dinnebier, R. Von Dreele, P.W. Stephens, S. Jelonek, and J. Sieler, J. Appl. Crystallogr. **32**, 761 (1999).

[21] D.N. Argyriou, J.F. Mitchell, P.G. Radaelli, H.N. Bordallo, D.E. Cox, M. Medarte, and J.D. Jorgensen, Phys. Rev. B **59**, 8695 (1999).

[22] N.W. Ashcroft and N.D. Mermin, *Solid State Physics* (Saunders College, New York, 1976), Chap. 32.

[23] R.L. Carlin, *Magnetochemistry* (Springer-Verlag, New York, 1986).

[24] H.A. Groenendijk, A.J. van Duyneveldt, and R.D. Willett, Physica B & C **98**, 53 (1979).

[25] J.A. Mydosh, *Spin Glasses: An Experimental Introduction* (Taylor and Francis, Washington, 1993).

[26] M.A. Subramanian, A.P. Ramirez, and W.J. Marshall, Phys. Rev. Lett. **82**, 1558 (1999).

[27] J.W. Stout and E. Catalano, J. Chem. Phys. **23**, 2013 (1955); W.O.J. Boo and J.W. Stout, *ibid.* **65**, 3929 (1976).

[28] J.N. McElearney, R.W. Schwartz, A.E. Siegel, and R.L. Carlin, J. Am. Chem. Soc. **93**, 4337 (1971).

[29] S. Sullow, G.J. Nieuwenhuys, A.A. Menovsky, J.A. Mydosh, S.A.M. Mentink, T.E. Manson, and W.J.L. Buyers, Phys. Rev. Lett. **78**, 354 (1997).

[30] A. Chakraborty, A.J. Epstein, W.N. Lawless, and J.S. Miller, Phys. Rev. B **40**, 11 422 (1989).

[31] A.M. Mulders, A. Yaouanc, P. Dalmas de Réotier, P.C.M. Gubbens, A.A. Moolenaar, B. Fåk, E. Ressouche, K. Prokeš, A.A. Menovsky, and K.H.J. Buschow, Phys. Rev. B **56**, 8752 (1997).

[32] T. Graf, M.F. Hundley, R. Molder, R. Movshovich, J.D. Thompson, D. Mandrus, R.A. Fisher, and N.E. Phillips, Phys. Rev. B **57**, 7442 (1998).

[33] N.P. Raju, J.E. Greedan, M.A. Subramanian, C.P. Adams, and T.E. Mason, Phys. Rev. B **58**, 5550 (1998).

[34] L.J. de Jongh and A.R. Miedema, *Experiments on Simple Magnetic Model Systems: A Survey of Their Experimental Status in the Light of Current Theories* (Barnes and Noble Books, New York, 1974).

[35] C. Domb and A.R. Miedema, in *Progress in Low Temperature Physics*, edited by C. J. Gorter (John Wiley and Sons, New York, 1964) Vol. IV, Chap. VI, p. 309.

[36] K. Kambe, S. Koide, and T. Usui, Prog. Theor. Phys. **7**, 15 (1952).

[37] H. Zhang, J.W. Lynn, W.-H. Li, T.W. Clinton, and D.E. Morris, Phys. Rev. B **41**, 11 229 (1990).

[38] J.W. Lynn, S. Skanthakumar, Q. Huang, S.K. Sinha, Z. Hossain, L.C. Gupta, R. Nagarajan, and C. Godart, Phys. Rev. B **55**, 6584 (1997).

[39] P.J. Brown, in *International Tables for Crystallograhy*, edited by A.J.C. Wilson (Kluwer Academic Publishers, Dordrecht, 1995), Vol. C, Chap. 4.4.5, p. 391.

[40] J.W. Lynn, J.A. Gotaas, R.N. Shelton, H.E. Horng, and C.J. Glinka, Phys. Rev. B **31**, 5756 (1985).

[41] Q. Li, J.W. Lynn, and J.A. Gotaas, Phys. Rev. B **35**, 5008 (1987).

[42] T. Fries, Y. Shapira, F. Palacio, M.C. Moron, G.J. McIntyre, R. Kershaw, A. Wold, and E.J. McNiff, Jr., Phys. Rev. B **56**, 5424 (1997).

[43] P. Burlet, E. Ressouche, B. Malaman, R. Welter, J.P. Sanchez, and P. Vulliet, Phys. Rev. B **56**, 14 013 (1997).

[44] F. Palacio, G. Antorrena, M. Castro, R. Burriel, J. Rawson, J.N.B. Smith, N. Bricklebank, J. Novoa, and C. Ritter, Phys. Rev. Lett. **79**, 2336 (1997).

[45] F. Palacio, M. Andriés, J. Rodriguez-Carvajal, and J. Pannetier, J. Phys.: Condens. Matter **3**, 2379 (1991).

[46] W. Opechowski and R. Guccione, in *Magnetism*, edited by G.T. Rado and H. Suhl (Academic Press, New York, 1965), Vol. IIa, Chap. 3, p. 138.

[47] P.W. Anderson, Phys. Rev. **79**, 705 (1950).

[48] J.B. Goodenough, *Magnetism and the Chemical Bond* (Wiley, New York, 1963).

[49] J. Kanamori, J. Phys. Chem. Solids **10**, 87 (1959).

[50] D.G. Wiesler, M. Suzuki, I.S. Suzuki, and N. Rosov, Phys. Rev. Lett. **75**, 942 (1995); D.G. Wiesler, M. Suzuki, I.S. Suzuki, and N. Rosov, Phys. Rev. B **55**, 6382 (1997).

[51] E. Ruiz, J. Cano, S. Alvarez, and P. Alemany, J. Am. Chem. Soc. **120**, 11 122 (1998); E. Ruiz, J. Cano, S. Alvarez, and P. Alemany, J. Comput. Chem. **20**, 1391 (1999).

[52] R. Sachidanandam, T. Yildirim, A.B. Harris, A. Aharony, and O. Entin-Wohlman, Phys. Rev. B **56**, 260 (1997).

[53] J.W. Lynn, I.W. Sumarlin, S. Skanthakumar, W.-H. Li, R.N. Shelton, J.L. Peng, Z. Fisk, and S-W. Cheong, Phys. Rev. B **41**, 2569 (1990); I.W. Sumarlin, J.W. Lynn, T. Chattopadhyay, S.N. Barilo, D.I. Zhigunov, and J.L. Peng, *ibid.* **51**, 5824 (1995).

[54] I.W. Sumarlin, S. Skanthakumar, J.W. Lynn, J.L. Peng, Z.Y. Li, W. Jiang, and R.L. Greene, Phys. Rev. Lett. **68**, 2228 (1992).

[55] I. Dzyaloshinsky, J. Phys. Chem. Solids **4**, 241 (1958); T. Moriya, Phys. Rev. **117**, 635 (1960); **120**, 91 (1960).

[56] A. Yoshimori, J. Phys. Soc. Jpn. **14**, 807 (1959).